



Combining remote sensing techniques and field surveys for post-earthquake reconnaissance missions

Giorgia Giardina¹  · Valentina Macchiarulo¹ · Fatemeh Foroughnia¹ ·
Joshua N. Jones² · Michael R. Z. Whitworth² · Brandon Voelker³ · Pietro Milillo^{3,4} ·
Camilla Penney⁵ · Keith Adams⁶ · Tracy Kijewski-Correa⁷

Received: 2 November 2022 / Accepted: 2 June 2023 / Published online: 30 June 2023
© The Author(s) 2023

Abstract

Remote reconnaissance missions are promising solutions for the assessment of earthquake-induced structural damage and cascading geological hazards. Space-borne remote sensing can complement in-field missions when safety and accessibility concerns limit post-earthquake operations on the ground. However, the implementation of remote sensing techniques in post-disaster missions is limited by the lack of methods that combine different techniques and integrate them with field survey data. This paper presents a new approach for rapid post-earthquake building damage assessment and landslide mapping, based on Synthetic Aperture Radar (SAR) data. The proposed texture-based building damage classification approach exploits very high resolution post-earthquake SAR data integrated with building survey data. For landslide mapping, a backscatter intensity-based landslide detection approach, which also includes the separation between landslides and flooded areas, is combined with optical-based manual inventories. The approach was implemented during the joint Structural Extreme Event Reconnaissance, GeoHazards International and Earthquake Engineering Field Investigation Team mission that followed the 2021 Haiti Earthquake and Tropical Cyclone Grace.

Keywords Remote reconnaissance · Remote sensing · Haiti · Building damage · Landslides classification · SAR · Texture analysis · Intensity ratio image

1 Introduction

Assessing building and infrastructure damage shortly after an earthquake is critical to support effective disaster relief management (Schweiher and Markus 2006). A rapid evaluation of the extent, intensity and distribution of damage needs to include both earthquake primary effects, i.e. the direct consequences of ground shaking, and secondary effects, of which landslides are the most impactful (Marano et al. 2010). Post-earthquake damage assessment is typically carried out by teams of experts deployed to the field. However, whilst in-situ examinations provide important knowledge (Aktas et al. 2022; Whitworth et al. 2022), field reconnaissance missions can be time-consuming and logistically

Extended author information available on the last page of the article

burdensome, especially for earthquakes affecting large regions, multiple state or country borders, or areas with challenging geopolitical circumstances.

Satellite-based remote sensing has been increasingly adopted in post-disaster management to overcome the limitations of in-situ reconnaissance. Optical and radar imagery can provide a safe and rapid overview of extensive affected areas, with radar data offering the further advantage of independence from weather conditions and daylight (Ge et al. 2020). However, the usefulness of advanced remote sensing techniques for post-earthquake assessment remains limited by the lack of a consistent framework for integrating field measurements and disparate remote sensing approaches, which are often context specific (Dong and Shan 2013).

In this paper we present a novel approach for the combined assessment of primary, i.e. building damage, and secondary, i.e. landslide, earthquake effects, based on the analysis of Synthetic Aperture Radar (SAR) data. The combined assessment addresses the need for comprehensive approaches that can be adopted in a multi-hazard scenario. We implemented this approach in parallel with field survey and satellite optical techniques during the joint StEER/GHI and EEFIT mission that followed the 2021 Haiti earthquake (Whitworth et al. 2022), where the seismic event impacted several urban areas, induced a large number of landslides and was followed by a tropical storm.

In Sects. 1.1 and 1.2 we introduce our proposed approach in the context of state-of-the-art satellite-based techniques for post-earthquake building and landslide assessment. Section 2 describes the Haiti 2021 earthquake case study, in which data were collected (Sect. 3) and our methodology was implemented (Sect. 4). Section 5 presents and discusses the results, and Sect. 6 summarises the main conclusions of this study.

1.1 Previous approaches to remote building damage assessment

Building collapse is responsible for 75% of all fatalities during earthquakes (Coburn et al. 1992). A rapid understanding of the extend of building damage and its spatial distribution is therefore critical to rescue operations and reconstruction efforts. Remote sensing techniques are increasingly being used to quickly assess the level and extent of structural damage in earthquake-affected areas (Joyce et al. 2009). At the same time, the use of such techniques in building damage assessment and disaster management has been formalised through initiatives such as the UNITAR Operational Satellite Applications Programme (UNITAR 2020).

The most common approaches use optical imagery to create damage assessment maps shortly after an event, e.g. Corbane et al. (2011). When weather conditions and daylight illumination allow it, optical imagery can be used for visual interpretation (Saito et al. 2005; Adams et al. 2005; Yamazaki et al. 2005; Ehrlich et al. 2009; Meslem et al. 2011; Fan et al. 2017) or automated change detection (Gamba and Casciati 1998; Yusuf et al. 2001; Janalipour and Taleai 2017). However, optical techniques are limited by the requirement for clear weather conditions and daylight illumination (Ge et al. 2020). More recent studies have, therefore, exploited the all-time, all-weather potential of Synthetic Aperture Radar (SAR) satellites. Comparing pre- and post-event backscatter intensity and phase information reveals changes in building characteristics, which can then be correlated with earthquake-induced damage (Matsuoka et al. 2010; An et al. 2016; Cui et al. 2018; Yun et al. 2015; Sharma et al. 2017).

Since these approaches rely on the difference between intensity and coherence of pre- and post-event SAR images, they cannot be used when pre-event images are not

available. This challenge has led to an increased demand for techniques using only post-event imagery, such as differences in backscattering, texture and bright areas (Dell'Acqua and Polli 2011; Zhao et al. 2013; Kuny et al. 2015; Wu et al. 2016; Gong et al. 2016; Bai et al. 2017; Ge et al. 2019). Such post-event studies are still limited (Ge et al. 2020), and more investigation is needed to exploit the recent launches of very high resolution (VHR) satellite constellations, as well as the possible complementary use of rapid field survey data.

In this work, we present a building damage classification approach based on texture analyses of post-earthquake VHR data acquired by the Capella SAR constellation over the urban area of Les Cayes, which was impacted by the 2021 Haiti earthquake. The proposed approach exploits VHR data that is made available only after a disaster, and it is integrated with the analysis of building survey jointly collected by StEER and GHI immediately after the 2021 event (Kijewski-Correa et al. 2021). The work represents a step forward in the combined use of new generation satellite data within the recently proposed framework of post-disaster hybrid reconnaissance missions (Aktas et al. 2022; Whitworth et al. 2022).

1.2 Previous approaches to remote landslide detection

Landslides are one of the the leading cause of fatalities induced by earthquakes' secondary effects (Marano et al. 2010). Understanding and mitigating these highly destructive events requires accurate techniques for the detection and mapping of landslides (Reichenbach et al. 2018; Froude and Petley 2018; Roback et al. 2018; Williams et al. 2018). While field techniques have been traditionally used to build landslide inventories, the temporal and logistical challenges currently limit their use to conduct detailed investigations of landslides with critical anthropogenic implications (Jones et al. 2020), or to validate limited portions of remotely developed inventories (Rabby and Li 2019), or to map regions where remote imagery is unavailable or of poor quality (Eeckhaut et al. 2007). As an alternative, extensive use has been made of remote sensing methods based on optical satellite data, using both manual (Harp and Jibson 1996; Massey et al. 2020) and semi-automated or automated approaches (Amatya et al. 2021; Hölbling et al. 2015; Lu et al. 2019; Mondini et al. 2011; Stumpf and Kerle 2011).

Semi- and fully automated landslide detection involves using statistical models, algorithms, or machine learning-based approaches to map landslides without the need for someone to individually delineate the boundaries of each separate landslide (Amatya et al. 2021; Hölbling et al. 2015; Lu et al. 2019; Mondini et al. 2011; Stumpf and Kerle 2011). The resulting faster mapping is particularly useful when landslide data are required at speed following a disaster event (Robinson et al. 2017). These methods also have the potential to be used to build up large-area multi-temporal databases that would be too time consuming and expensive to develop manually. A typical semi-automatic landslide detection and mapping scheme involves the development of index-based change maps that automatically highlight landslide attributes relative to the rest of the landscape. For example, Normalised Difference Vegetation Index (NDVI) or Brightness Index (BI) percentage change maps can be automatically derived from a variety of multi-spectral satellite inputs (Scheip and Wegmann 2021) before applying simple thresholds or classification techniques to try and separate out specific landslide boundaries (Amatya et al. 2021; Close et al. 2021; Ma et al. 2016; Hölbling et al. 2015; Rau et al. 2014).

One issue that commonly affects both manual and semi- or fully-automated remote sensing-based landslide detection techniques is cloud cover (Lacroix et al. 2018; Robinson

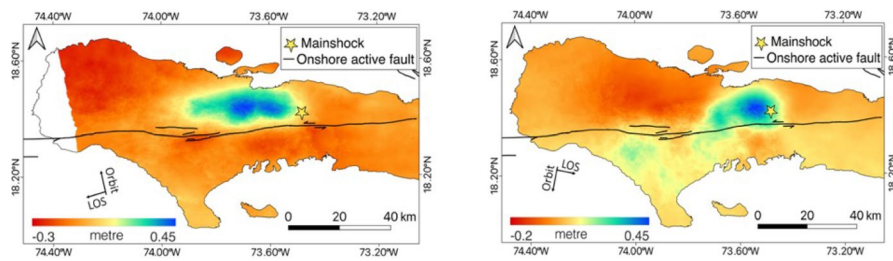
et al. 2019), as the optical imagery used to develop indices such as NDVI and BI are unable to penetrate cloud. This is problematic in many landslide prone locations such as Nepal and Haiti, and can render such methods useless if rapid post-disaster detection is needed (e.g., because it is not possible to wait for cloud-free images to be available). One solution to this is to use methods using wavelengths that are capable of penetrating cloud cover such as SAR. Furthermore, the radar signal is sensitive to ground surface properties, roughness, and moisture content (Aimaiti et al. 2019), making it possible to observe changes on the ground due to landslide scars between two SAR acquisitions (Burrows et al. 2019).

In the past decades, SAR data have played an important role in landslide detection (Colesanti and Wasowski 2006; Hilley et al. 2004; Greif and Vlcko 2012; Bianchini et al. 2012; Konishi and Suga 2018). However, most of the available literature focuses on the development of Interferometric SAR (InSAR) techniques, where ground surface deformation is estimated from the differences in phase content of the radar signal between subsequent acquisitions (Handwerger et al. 2019; Huang et al. 2017; Intrieri et al. 2018; Schlögel et al. 2015). Only a limited number of studies are currently available on the use of backscatter intensity variations to detect changes on the ground surface that can be correlated to earthquake-induced landslides (Mondini et al. 2019). Recently, new methodologies have been proposed using freely available data, e.g. from Sentinel-1, processed directly on free cloud-based online platforms such as Google Earth Engine (GEE), to incentivise a widespread use of backscatter intensity data for rapid landslide detection (Handwerger et al. 2022). However, these approaches have so far only been used to highlight areas with high density of landslides, and have not been widely applied to actual landslide mapping and classification in an operational scenario.

In this paper, we build on these recent advances in backscatter intensity-based landslide detection in order to classify landslides triggered by the 2021 Haiti earthquake. Both unsupervised and supervised methods are applied to the intensity ratio image generated by using multi-temporal stacks of Sentinel-1 data extending over the earthquake date. A classification method to separate landslides from flooded areas is included, and quantitative comparison of the classification results are made with optical-based manual inventories.

2 The 2021 Haiti earthquake

The Mw 7.2 Nippes earthquake occurred on 14 August 2021, at 8:29 am Eastern Daylight Time (Haitian Local Time). Figure 1 shows the earthquake-induced surface displacement maps (Whitworth et al. 2022). The earthquake epicentre was slightly to the north of the mapped trace of the Enriquillo–Plaintain-Garden fault, which runs approximately east–west along the Tiburon peninsula in south-east Haiti (Saint Fleur et al. 2020). This fault has been mapped, and included in hazard maps, as vertical and left-lateral (Frankel et al. 2011) but the earthquake had both strike-slip and reverse components, possibly in two sub-events (Calais et al. 2022; Okuwaki and Fan 2022; Maurer et al. 2022). This complex faulting emphasises the need, first made clear in the Mw 7.0 earthquake which struck Haiti’s capital, Port-au-Prince, in January 2010, for a more detailed understanding of the tectonics and faulting of Hispaniola, and southern Haiti in particular. The largest aftershock of the 2021 earthquake was a Mw 5.7 event the day after the mainshock. In combination with Tropical Cyclone Grace, which skirted Haiti on 16 August 2021, these events triggered several thousand landslides (Martinez et al. 2021) and caused extensive flooding across the study area (see Sect. 5.2 on landslide detection below).



(a) Sentinel-1 ascending, images acquired on 5 August and 17 August 2021

(b) Sentinel-1 descending, images acquired on 3 August and 15 August 2021

Fig. 1 Surface displacement maps obtained by processing a pair of SAR Sentinel-1 images acquired before and after the earthquake (Whitworth et al. 2022). The yellow star indicates the earthquake epicentre. Black lines are onshore active faults from Saint Fleur et al. (2020). LOS indicates the satellite Line Of Sight

The estimated death toll from the Nippes earthquake was 2000, with a further 15,000 injured (UN OCHA 2021). This death toll is two orders of magnitude lower than that for the 2010 earthquake, despite the 2021 earthquake releasing approximately twice as much energy. This is largely due to the epicentre of the 2021 event being much further from the major population centre of Port-au-Prince and the fact that the housing stock in the affected regions is mostly single storey constructions (Kijewski-Correa et al. 2021). The recovery from the 2010 earthquake, both in terms of the enormous death toll and the associated economic impacts, was ongoing at the time of the 2021 earthquake. In addition, in 2016 Hurricane Matthew caused severe damage across much of Haiti, including the departments affected by the 2021 earthquake. As a result, the recovery needs of US\$ 1.98 billion estimated in the Post-Disaster Needs Assessment (PDNA) will compound an already strained financial situation (UNDP 2015). The coincidence of the Nippes earthquake with the Covid-19 pandemic and ongoing political instability in Haiti emphasised the need to rapidly collect perishable post-earthquake data using remote methodologies (Whitworth et al. 2022).

3 Data

Following the earthquake, the StEER/GHI team deployed a hybrid response mission by mobilising local non-experts to record building damage (Kijewski-Correa et al. 2022) and coordinating with teams of experts operating remotely, e.g. the Earthquake Engineering Field Investigation Team (EEFIT), for the assessment of photographic materials and the collection and processing of remote sensing data (Whitworth et al. 2022).

3.1 Building data

The StEER/GHI Fulcrum dataset (Kijewski-Correa et al. 2022) included the approximate geolocation, relevant photographs, and assigned damage level of 11,669 buildings. Among these, 215 records fell into the defined area of interest over Les Cayes (Fig. 2). Each assessed building was classified according to its structural typology. These classes were: Reinforced Concrete with infill masonry shear walls (RC), Confined Masonry (CM), Unreinforced Masonry bearing walls (URM), Reinforced Masonry bearing walls (RM), Wood

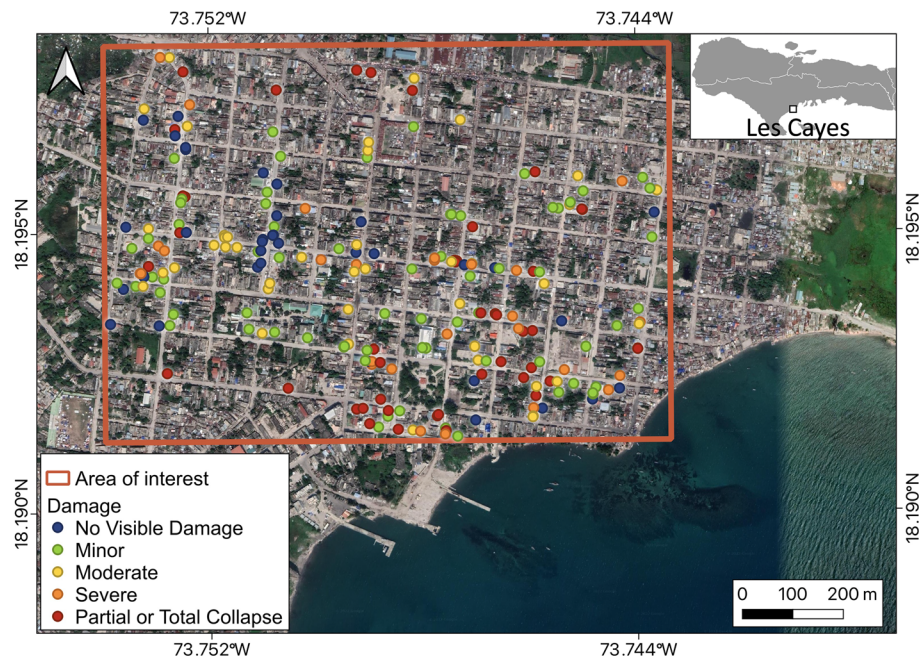


Fig. 2 StEER/GHI Fulcrum dataset over the area of interest in Les Cayes

Light frames (WL), Wood with Stone infills (WS), and Unknown (UN). The damage level was rated as No Visible Damage, Minor, Moderate, Severe and Partial or Total Collapse (Miranda 2021).

For the SAR-based damage assessment we used a single Capella-5 (Stringham et al. 2019) Very High Resolution (VHR) X-band SAR image that was acquired over Les Cayes, Haiti, on 16 August 2021, 2 days after the mainshock. The Capella post-event SAR image was acquired in Spotlight mode from a descending pass with a look angle of 48.8° and HH polarization. The image has range and azimuth resolutions of 0.59 m and 0.63 m respectively, and covers an area of $5 \times 5 \text{ km}^2$. Range-compression, detection, focusing, multi-looking, and terrain-height correction were already performed by the provider. Specifically, a multi-looking factor of 1×9 (range \times azimuth) was used to enhance radiometric resolution.

3.2 Landslide data

To allow for a comparison between the SAR data with optical-based manual inventories, Sentinel-2 optical data were obtained from the USGS Earth Explorer (USGS 2022) for the landslide region of interest for a pre- and post- event time slice with as little cloud as possible. The pre-event imagery was taken on 4 August 2021, whilst the post-event imagery was taken on 14 August 2021, the day of the earthquake. Sentinel-2 sensors comprise 13 spectral bands with spatial resolutions of 10–60 m and re-visit times (temporal resolution) of 2–5 days depending on latitude. This makes Sentinel-2 data ideal for landslide mapping,

as the short temporal resolution and high spatial resolution allow for the identification of medium to large ($> 100 \text{ m}^2$) landslides at short timescales following a triggering event.

Sentinel-1 C-band SAR data in high resolution Ground Range Detected (GRD) format were obtained from GEE as backscatter intensity coefficient images in 10 m pixel spacing resolution. We also used Sentinel-1 data in Interferometric Wide Swath (IW) mode. The backscatter intensity coefficient is defined as the target backscattering area (radar cross-section) per unit ground area. GRD products consist of intensity data only and provide information on the changes in the ground surface. They are multi-looked, radiometrically calibrated, and terrain-corrected using an Earth ellipsoid model (GEE 2022). In this study, two stacks of 1169 ascending (i.e., 1117 pre-event and 49 post-event) and 618 descending (i.e., 579 pre-event and 31 post-event) GRD VH polarization products, acquired before and after a 7-day window which included the earthquake date, were obtained from GEE.

4 Methodology

4.1 Building damage assessment

For this work we processed the post-event Capella SAR image through the SNAP Sentinel-1 toolbox (SNAP 2022) to extract Grey Level Co-occurrence Matrix (GLCM) texture features (Haralick et al. 1973). To estimate the GLCM texture features we used a window size of $15 \times 15 \text{ m}^2$. Given the high resolution of the data (about 50x50 cm in range and azimuth), this value was comparable with the average size of buildings in the study area, which is about 100 m^2 on average. The selected window size is also in line with previous studies (Kuny et al. 2015; Zhao et al. 2013). Since we were not interested in the directionality of the textures, the GLCM features were computed along several directions, i.e., 0° , 45° , 90° and 135° , and results from different directions were averaged. We estimated a total of ten texture features: contrast, dissimilarity, homogeneity, Angular Second Moment (ASM), energy, maximum probability (MAX), entropy, mean, variance, and correlation.

To identify the texture features that are better correlated with damage, we analysed each feature in relation to ground truth data, i.e., the StEER/GHI Fulcrum dataset. First, we assigned each Fulcrum damage record to the corresponding building footprint. Depending on data availability in the analysed area, the proposed approach can be used with different building footprint maps, such as OpenStreetMap (OSM 2021) and Microsoft Building Footprints (Microsoft 2023), or more detailed datasets provided by local authorities. Since a cadastral dataset was not available for our study area and the OpenStreetMap building dataset for Les Cayes is not sufficiently accurate, building footprints were digitised manually in a Geographical Information System (GIS) environment for a region in central Les Cayes (Fig. 2). We used a 2-cm-resolution, post-event orthophoto that was acquired by aerial drone on 18 August 2021 and released by HaitiData (HaitiData 2021), a web-based platform developed after the 2010 Haiti earthquake to disseminate GIS and other cartographic data in support of disaster management. To deal with the shape of totally or partially collapsed buildings, an 8-cm-resolution drone orthophoto dated back to October 2016 was also used. This resulted in the mapping of a total of 4116 building footprints. For each texture, pixels belonging to the buildings assigned to the StEER/GHI Fulcrum dataset were classified according to the corresponding damage level. This was useful for identifying the most representative texture features to be used for the final damage classification.

To highlight areas with different concentrations of heavily damaged structures, we divided our area of interest into 75 city blocks, with an average of 48 buildings per block. We considered a city block as the smallest group of buildings that is surrounded by streets, and therefore derived the city blocks from the OpenStreetMap road network (OSM 2021). Notably, the reflections associated with open spaces, e.g., car park, bare ground, and vegetation present within a specific block, can have a large impact on the average texture (Dell'Acqua and Polli 2011). For example, the textural signature of heaps of debris and high vegetation can be very similar (Kuny et al. 2015). To mitigate the impact of vegetation and open spaces on the final damage classification, only the pixels within building footprints were used to estimate the average texture within the corresponding block. This approach also mitigates the possible influence of city block size on the final results, as long as there are no city block including only a few buildings. City blocks were then classified into five damage classes, based on the averaged value of the relevant texture feature computed within the block. The five damage levels, from 1 to 5, were labelled as “very low”, “low”, “intermediate”, “high” and “very high”.

4.2 Landslide detection

For the first stage of the optical-based landslide detection methodology, we developed a fully manual inventory of earthquake-induced landslides from the Sentinel-2 imagery. This was done by processing the imagery to false colour RGB images with the red band set to the near-infrared multispectral band and the green and blue bands kept to the green and blue multispectral bands. The pre- and post-event imagery was then inspected to locate bare-earth features that appeared between the timeslices. Landslides bare earth attributes were distinguished from characteristics related to other processes, such as anthropogenic land-use change relating to road cuts, deforestation or land clearing, or fluvial processes such as channel bank erosion. Each feature identified as a landslide was delineated within a GIS environment as a polygon that included the source, runout, and deposition zone of each landslide. Care was taken to avoid landslide amalgamation, where multiple intersecting landslides can be erroneously mapped as one single polygon (Marc and Hovius 2015). Finally, we exported all identified landslides into a single shapefile, which constitutes the final landslide inventory.

In the second stage of the optical-based landslide detection methodology, we implemented a semi-automatic mapping process. We used a GIS raster composite band function to create rasters that included only the multispectral bands required for (a) Normalised Difference Vegetation Index, NDVI (visible and near-infrared, B8, and red, B4), and (b) Brightness Index, BI (red, B4, and green, B3) calculations, for both the pre-event and post-event imagery. These bands were then combined using the following equations to obtain pre- and post- event rasters of NDVI and BI (SNAP 2022):

$$NDVI = \frac{(B8 - B4)}{(B8 + B4)}; BI = \frac{(B4 \times B4) + (B3 \times B3)}{2} \quad (1)$$

We then subtracted the pre-event from the post-event imagery for both the NDVI and BI outputs to obtain NDVI and BI change maps, before running an unsupervised classification on both change maps. The unsupervised method allows the classification model to automatically determine how many classes to classify the change map inputs into. For the NDVI change map, the unsupervised classifier defined four classes, whilst it defined eight classes for the BI change map. In both cases we then manually defined a landslide class

from the pre-defined classes (i.e., the class that most closely matched the known landslide locations), plus various other landscape or cloud related classes.

Finally, to overcome the cloud coverage limitations of optical data, we implemented a landslide classification based on a SAR intensity ratio image. For the SAR backscatter intensity-based analysis we combined a stack of pre-event backscatter intensity images from 2015 to the event date (14 August 2021) and a stack of 2-month post-event backscatter intensity data from 7 days after the event (21 August–13 October 2021). For each stack we first calculated the median of the pre- and post-event SAR backscatter intensity VH data, for both the ascending and descending geometries. Then, the average of both geometries' backscatter intensity coefficient I was calculated for both the pre- and post-event stack (I_{pre} and I_{post}). Finally, the intensity ratio describing the change in backscatter intensity coefficient was calculated (Handwerger 2022a; Handwerger et al. 2022):

$$I_{\text{ratio}} = 10 \times \log_{10}(I_{\text{pre}}/I_{\text{post}}) \quad (2)$$

On the resulting intensity ratio image, we initially applied unsupervised classification, with the aim of performing a rapid separation of landslides from the surrounding areas. For the unsupervised classification we used the Expectation Maximization (EM) Cluster algorithm embedded in the SNAP Sentinel-1 toolbox (SNAP 2022). EM is a generalisation of the k-means algorithm where each cluster is defined by an ellipsoid with a centre and covariance matrix. The algorithm minimises the intra-cluster variances iteratively, and is independent of different scales of data dimensions and their correlations (Dempster et al. 1977). Random seed points are used to initialise the pseudo-random number generator of the initial cluster.

To classify the landslides more accurately and separate landslides from water areas, we later applied supervised Random Forest (RF) classification (Breiman 2001). The RF classifier was applied to fourteen different features. Twelve of these features were derived from SAR data, and include: intensity ratio image, ten GLCM textural features from intensity ratio image, and a combination of SAR VV and VH backscatter data from ascending and descending acquisition geometries. Two features, slope and aspect, were derived from a 30-m-resolution Shuttle Radar Topography Mission (SRTM). The GLCM features were obtained by using a relatively small window size of 5 pixels, to increase the possibility of detecting small landslides. For the combination of SAR VV and VH backscatter data from different acquisition geometries, first we calculated the temporal median images of both ascending (17 August 2022 and 23 August 2022) and descending data (15 August 2022 and 21 August 2022), and then we averaged the median images.

To account for the flood event that occurred 2 days after the earthquake (see Sect. 2), in the supervised classification we explicitly included the flood water as an additional class, leading to the classification of three classes: landslides, flood water and others. To train the model and then evaluate the classification, samples were collected using the manually derived polygons from the optical imagery mapping (Sentinel-2 data acquired on 4 August 2021 and 14 August 2021) and Sentinel-2 data acquired on 19 August 2021. The latter date was selected for its limited cloud coverage, in order to complement the optical-based manual inventory. Additionally, and specifically for a more accurate collection of water samples, the Normalized Difference Water Index (NDWI) (McFeeters 1996) obtained from Sentinel-2 data was used as an indicator of changes in water content. The Sentinel-2 data were acquired on 19 August 2021, i.e. 3 days after cyclone Grace skirted Haiti.

Finally, to reduce the noise due to misclassification effects, we applied a Sieve filter implemented in the Geospatial Data Abstraction Library (GDAL/OGR contributors 2020)

to the results of both the unsupervised and supervised classifications. This filter removes raster polygons smaller than a predefined threshold size (in pixels) and replaces them with the pixel value of the largest neighbour polygon.

5 Results

5.1 Building damage assessment

The relationship between the ten texture features derived from the post-event Capella SAR image and the five damage levels used to rate the StEER/GHI Fulcrum records were analysed with box plots, as shown in Fig. 3. A boxplot is a method used in descriptive statistic to show the distribution of data groups by dividing the number of data points within each group into four parts of equal size, or quartiles. In each boxplot, the box identifies the range where 50% of data values lay, and ranges between the 25th percentile of data, or lower quartile, and the 75th percentiles of data, or upper quartile. The lines extending from the box, called whiskers, show the distribution of data values outside the upper and lower

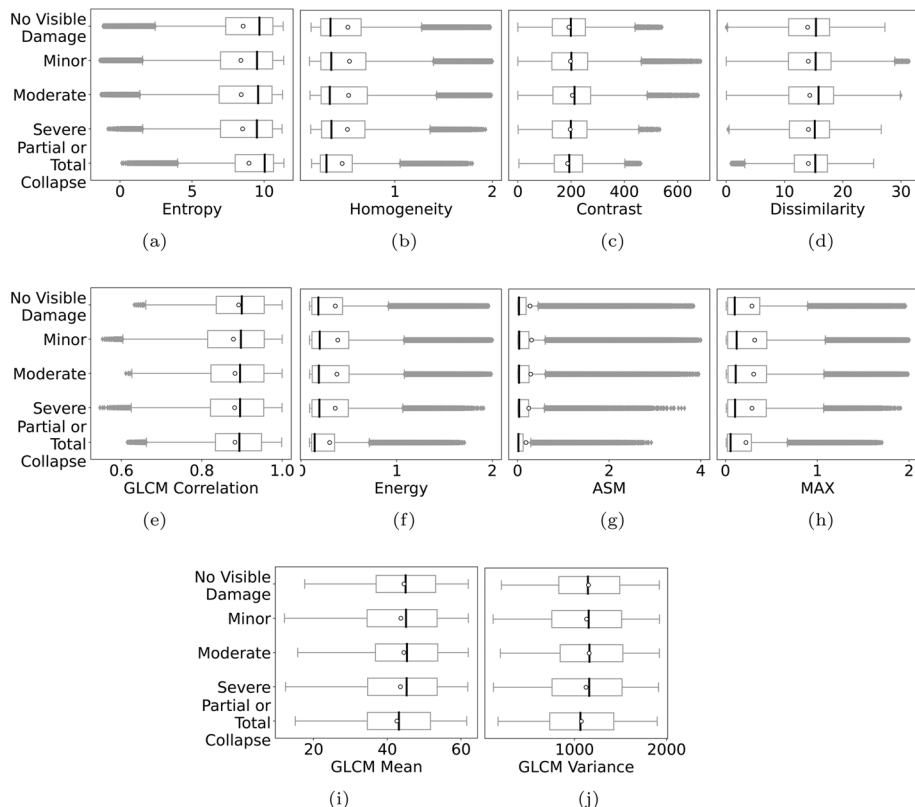


Fig. 3 Box plot relationships between Capella-based texture features and StEER/GHI Fulcrum damage levels. In each box, the round and the flat central markers indicate the mean and the median values, respectively. Diamond markers indicate outliers. The box edges correspond to the 25th and 75th percentiles

quartiles. Each whisker identifies a range where about 25% of data values lay. All values that differ significantly from most of the data, i.e., outliers, are plotted as individual points beyond the whiskers. The minimum and maximum correspond to the lowest value (excluding the outliers) at the end of the left whisker, and the highest value (excluding the outliers) at the end of the right whisker, respectively. The vertical line that divides the box in two parts is the median or middle value in the data, while the circle inside the box corresponds to the mean or average value.

For each texture feature, texture pixel values associated with buildings surveyed in central Les Cayes were classified according to the corresponding Fulcrum damage level. Figure 3 shows that an increase in average entropy (Fig. 3a) and a decrease in average homogeneity (Fig. 3b) values can be connected with ‘Partial or Totally Collapsed’ buildings. This is because, for collapsed structures, a reduced regularity that causes an increase in disorder, i.e. entropy, and conversely a decrease in homogeneity, is expected in the SAR backscatter intensity image. These observations are also in line with previous studies (Dell’Acqua and Polli 2011; Zhao et al. 2013) and can be explained by the large texture variation exhibited by the collapsed portion of the structure. Additionally, the vertical or semi-vertical perspective of the satellites can limit their capability to identify minor damage, damage within structures, and cracks on the walls. While the specific range of values in Fig. 3 are data-dependent, as the GLCM textures describe the frequency in the spatial relationships between pixels in a neighbourhood, similar trends can be expected in different events (Hall-Beyer 2017).

Figure 4 shows the classification results at the city block level based on the entropy texture derived from the post-event Capella SAR image. The map represents the distribution of average entropy values within each block. City blocks associated with low entropy values are likely characterised by a low density of damaged buildings, while high entropy values likely indicate a high concentration of damaged structures. We found that for 11% of city blocks the average entropy level is very low, for 20% of city blocks the average entropy is low, 39% of city blocks show an intermediate level of average entropy, for 21% of blocks the average entropy is high, and for 9% of them the average entropy texture is very high.

The results of the entropy-based damage classification were analysed in combination with the StEER/GHI Fulcrum records and a 2-cm-resolution drone-based orthophoto acquired on 18 August 2021. For example, Fig. 5 shows a close-up of a city block characterised by a very low level of average entropy texture. A comparison with the StEER/GHI Fulcrum records available for some of the buildings within the same block shows that the surveyed structures are characterised by ‘Minor’ or ‘Moderate’ damage level, showing a good correlation with the corresponding entropy class. Figure 6 shows an example of city block characterised by very high average entropy, likely indicating that the block was heavily damaged during the earthquake. A visual comparison with an aerial orthophoto shows that several large buildings within the block were partially or totally collapsed, correlating well with the very high entropy class.

5.2 Landslide detection

Figure 7 shows the final landslide inventory derived from the manual mapping using optical satellite imagery. In total 477 landslides were delineated with a total area of 15.9 km². As is clear from Fig. 7, there is a large area where mapping was not possible due to the cloud cover.

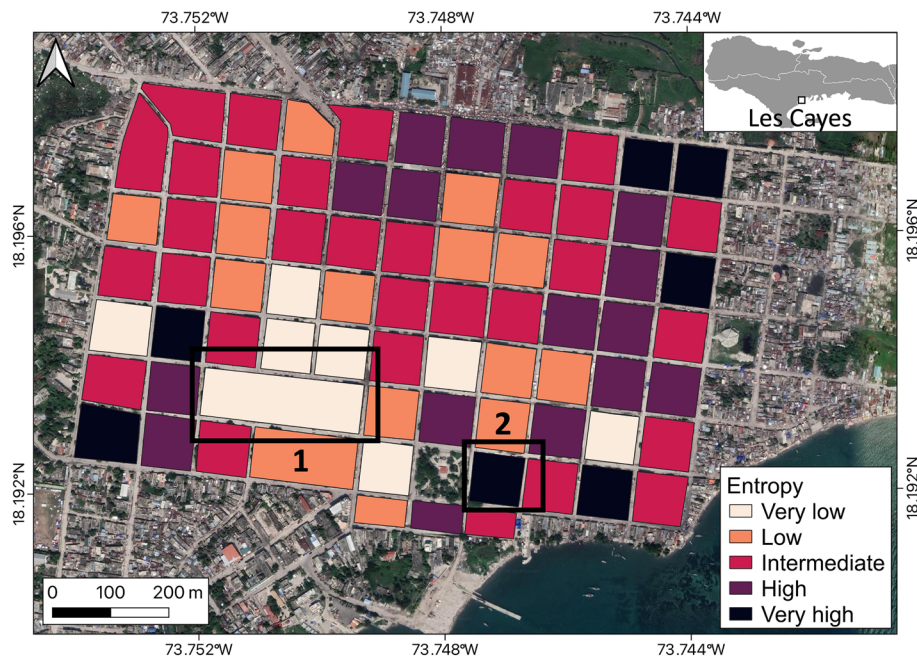


Fig. 4 Entropy-based damage classification at the city block level in central Les Cayes, Haiti. Increasing entropy is likely correlated with increasing damage. The entropy texture was derived from a Capella SAR image acquired on 16 August 2021. The areas highlighted by the rectangles 1 and 2 indicate two regions for which a closeup is given in Figs. 5 and 6, respectively

Figures 8 and 9 show the final NDVI and BI change maps, whilst Figs. 10 and 11 show the results of the unsupervised classifications. It is evident that whilst the NDVI change map (Fig. 8) does allow visual detection of landslides, the unsupervised classification applied to this map (Fig. 10) was unable to sufficiently delineate landslides relative to other image features such as clouds. Conversely, whilst it is slightly harder to visually identify landslides in the BI change map (Fig. 9), the unsupervised classification applied to this map (Fig. 11) is more accurate at delineating landslide boundaries relative to other features. However, the BI classification still cannot fully distinguish landslides from clouds. Furthermore, in both cases, in common with the manual approach, the presence of clouds makes mapping using this method impossible for much of the study region.

To mitigate the issue of cloud coverage in optical data, we also implemented classification approaches based on SAR intensity ratio image. Figure 12 shows the 7-day intensity ratio image of the landslide area of interest.

First, we applied the EM unsupervised classification to the SAR intensity ratio image, in order to distinguish landslides from non-landslide areas. A different number of seed and iteration parameters were tested, leading to the final selection of 100 seeds and 30 iterations. Figure 13 shows that the EM Cluster algorithm appeared to isolate pixels associated with landslides reasonably well. However, flood water areas were wrongly classified as landslides, as similar SAR reflections were observed in the intensity ratio image. Table 1 shows the confusion matrix of the unsupervised classification results.

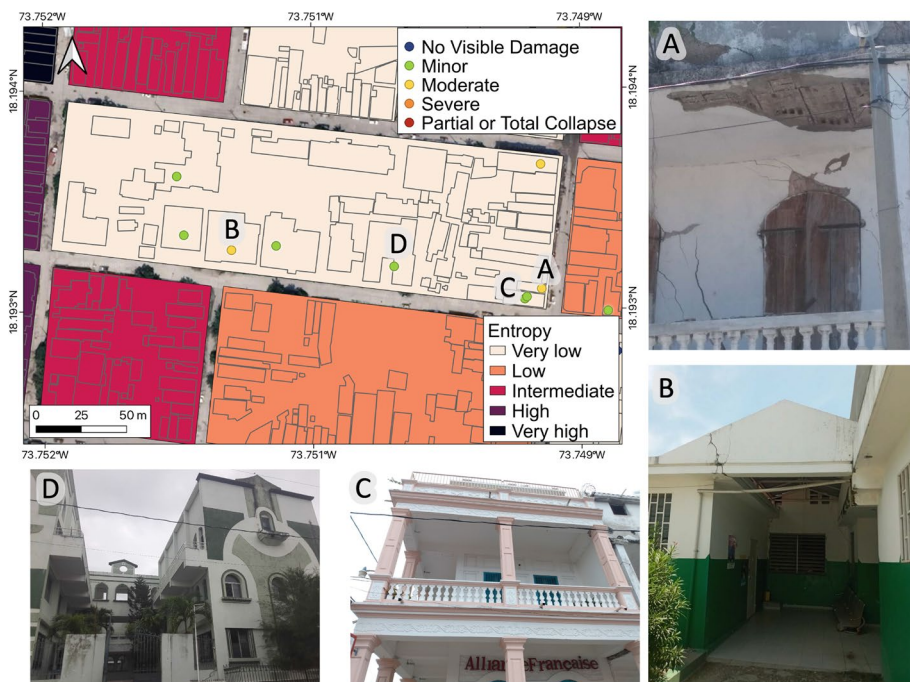


Fig. 5 Close up to a city block showing a very low level of average entropy texture in overlap with StEER/GHI Fulcrum records. The close up corresponds to the area 1 highlighted in Fig. 4. Photographs A, B, C, and D correspond to buildings surveyed as part of the StEER/GHI hybrid response. Building footprints within each block are outlined in grey

For this reason, we also performed a Random Forest (RF) supervised classification. The textural and SRTM-derived features were included in the classification procedure to increase the possibility of separating landslides from flood water areas. A RF classifier with 150 trees was applied to the SAR and SRTM-derived features (see Sect. 4). We used a total of 41,553 samples: 70% (29,069) and 30% (12,484) of the samples (Fig. 14) were used for training the classifier and evaluating the classification results, respectively. We used 10,556 training samples for the landslide class, 15,554 for the non-landslide class and 2,959 training samples for the water class. The training model has an accuracy of 0.97 for landslides, 0.95 for non-landslides and 0.98 for water. Figure 15 shows the classified map obtained from the RF classification. It is clear that the supervised classification approach helped to discriminate flood water areas from landslides. Additionally, if compared with the unsupervised result, the landslide extents appear to be more accurately delineated.

Table 2 shows the confusion matrix of the RF classification result.

The overall accuracy of approximately 83% was obtained, indicating good performance of the RF classifier in landslide mapping for this case study. Generally, the water and non-landslide areas were reasonably well classified; however, some misclassifications of landslides and non-landslide areas with water were observed in the results. The misclassification of non-landslide and water areas can be related to the saturation of agricultural fields within the area of interest, which is likely a consequence of the flood event.



Fig. 6 Close up to a city block showing a very high level of average entropy texture. The close up corresponds to the area 2 highlighted in Fig. 4. Imagery data A, B, C, and D correspond to buildings visually inspected in a 2-cm-resolution drone orthophoto acquired on 18 August 2021. Building footprints within each block are outlined in grey

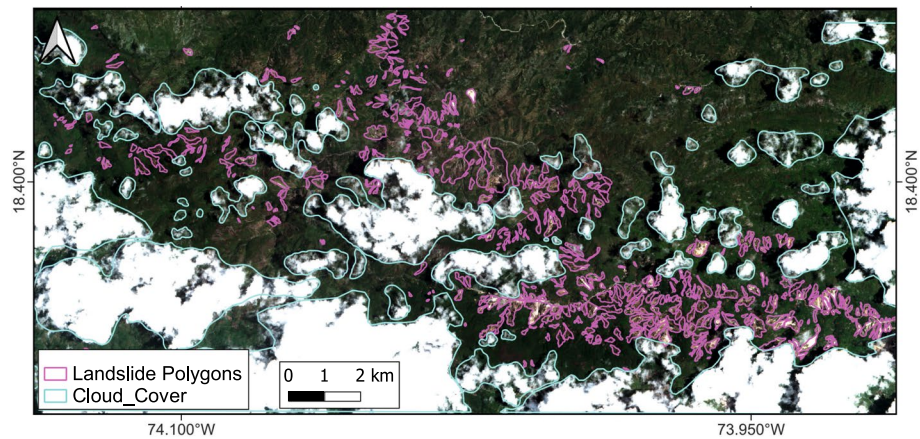


Fig. 7 Optical manual landslide inventory map

The same testing samples were also used to evaluate the results obtained from the unsupervised classification. The overall accuracy was approximately 75%, with only 53% correct landslide pixels. The comparison, detailed in Table 3, indicates a lower performance of the unsupervised classification. As such, following a combined earthquake and flood scenario, unsupervised classifications such as this should be used only for

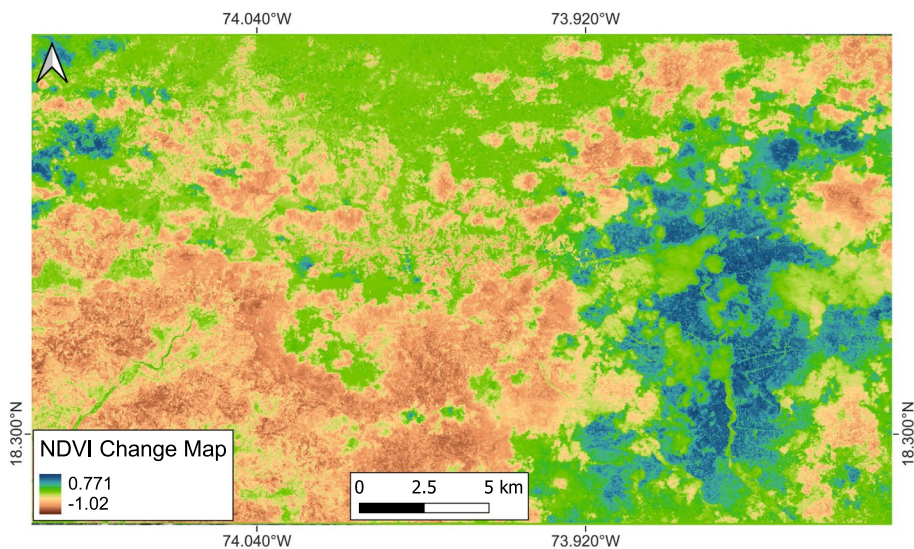


Fig. 8 NDVI change map generated from difference in NDVI between pre- and post-event Sentinel-2 imagery

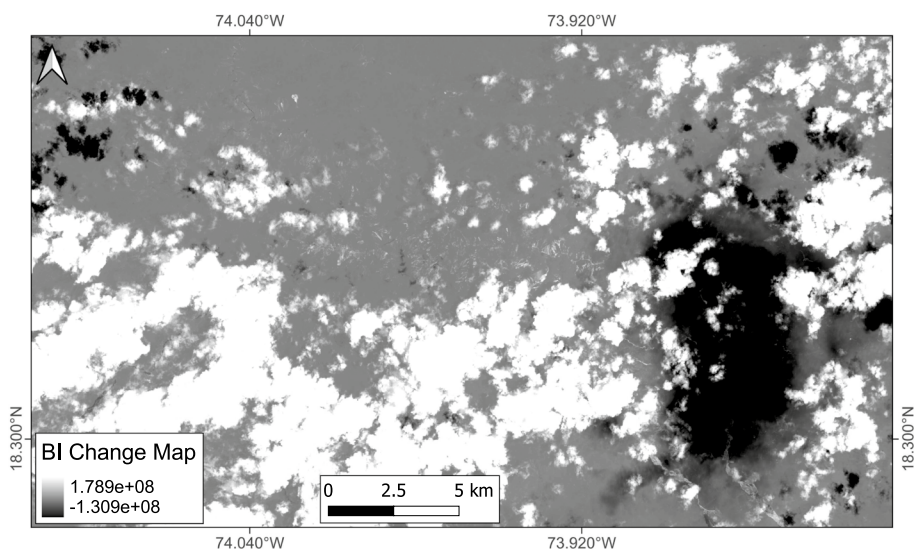


Fig. 9 BI change map generated from difference in NDVI between pre- and post-event Sentinel-2 imagery

rapid overview assessments. Whenever testing and training data is available, supervised classification of intensity ratio images rapidly obtained from free online cloud-based platforms can guarantee a better level of accuracy. This approach also shows promise for developing multi-temporal landslide inventories over large areas, which are becoming

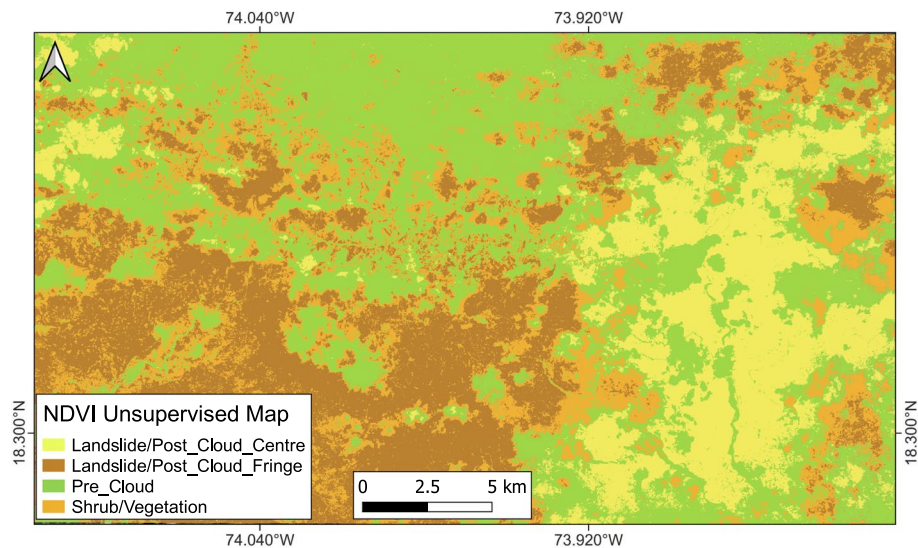


Fig. 10 Unsupervised classification of NDVI change map. Note that it cannot distinguish cloud and landslides

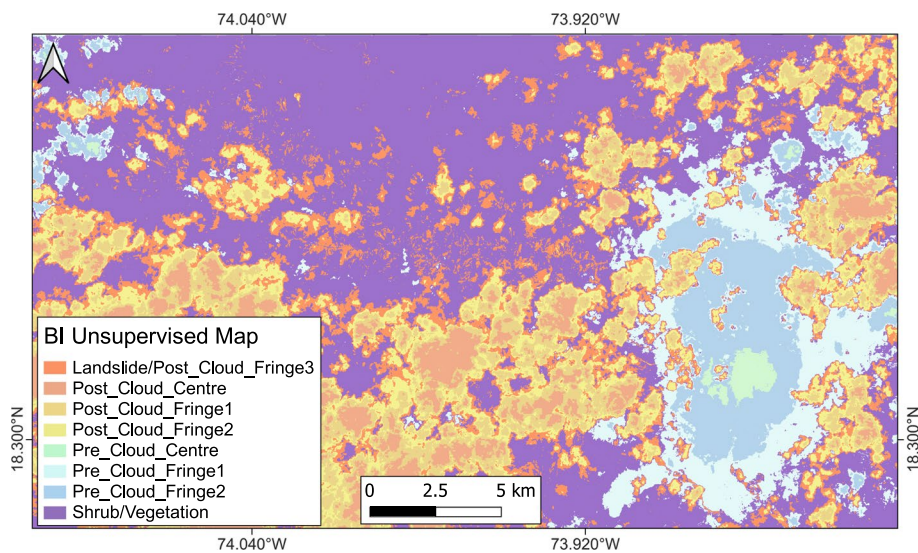


Fig. 11 Unsupervised classification of BI change map. Note that it has better capabilities to distinguish cloud and landslides, but cannot fully delineate them, with cloud fringes still showing as landslides

increasingly important given recent findings pertaining to landslide time-dependency (Marc et al. 2015; Parker et al. 2015; Jones et al. 2021a, b; Roberts et al. 2021; Samia et al. 2017).

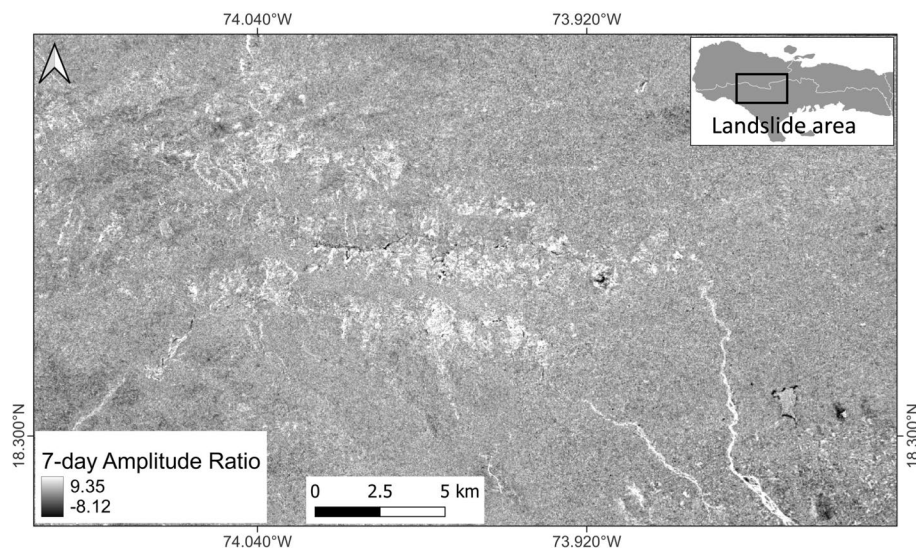


Fig. 12 Intensity ratio image over the landslide area of interest

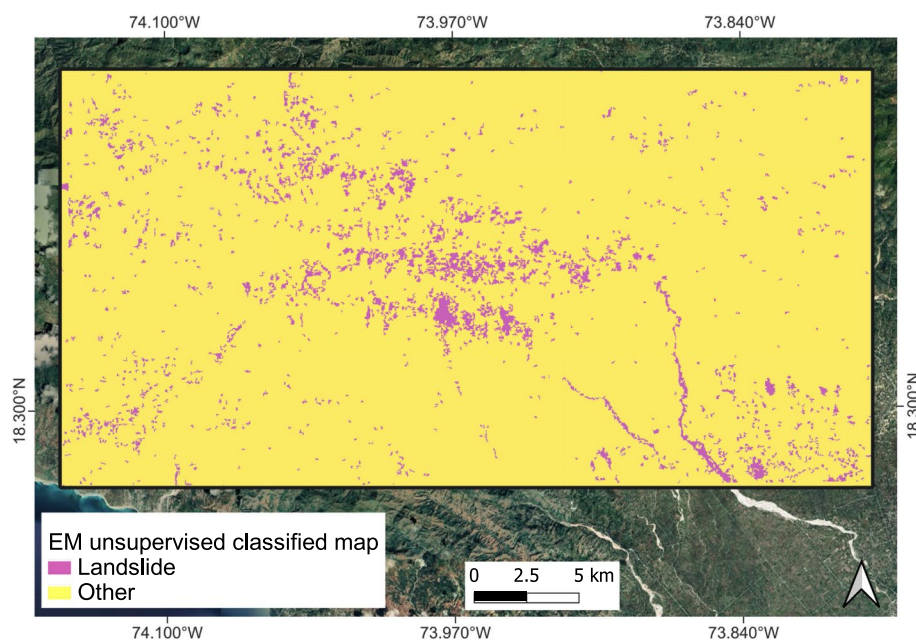
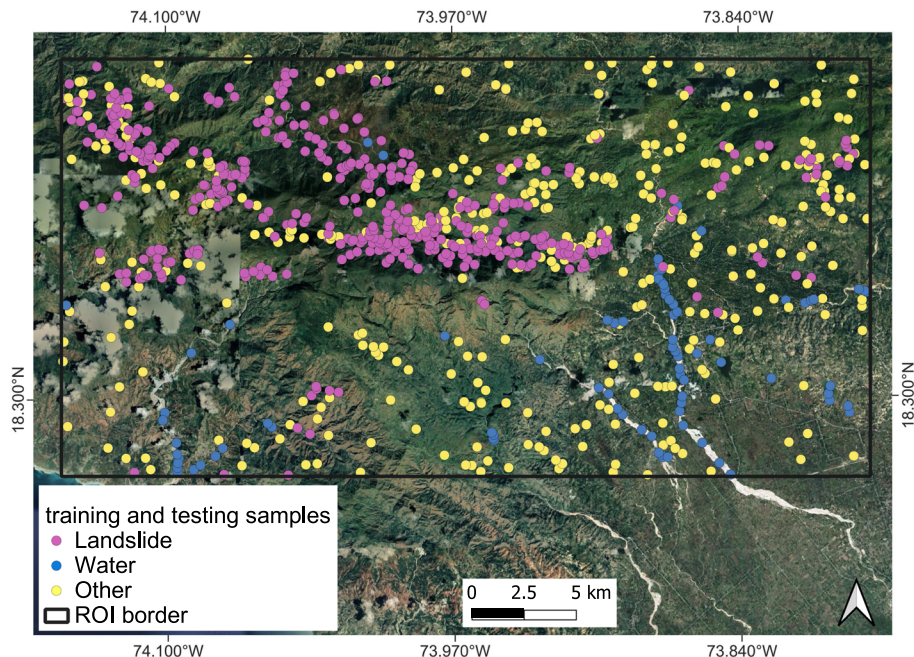


Fig. 13 EM unsupervised classification map

Table 1 Unsupervised classification confusion matrix

	Predicted classes		
	Landslide	Non-landslide	Total
<i>Actual classes</i>			
Landslide	1968	1752	3720
Non-landslide	663	6465	7128
Total	2631	8217	10,848

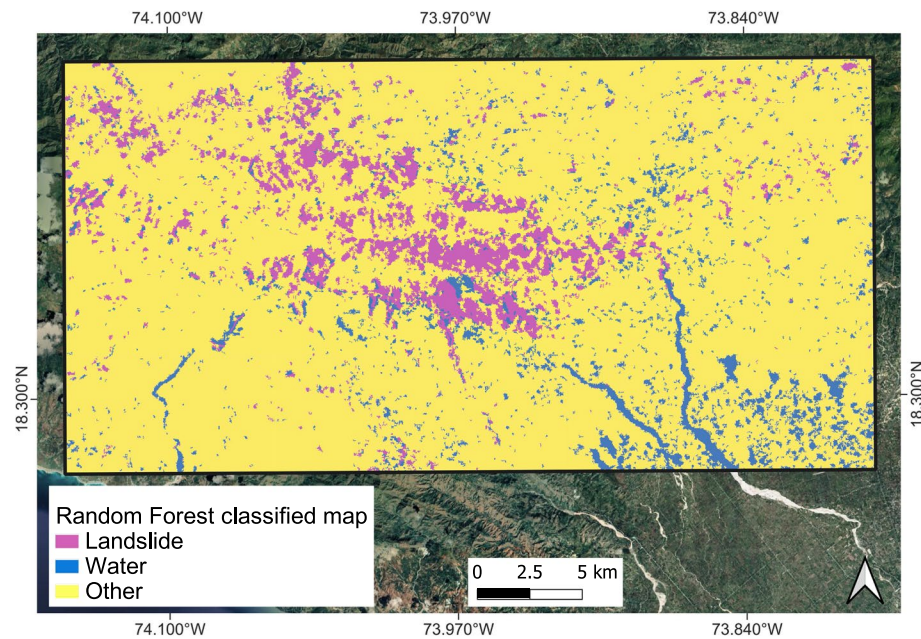
**Fig. 14** Distribution map of training and testing samples collected for the RF supervised classification. Each point indicates the centroid of the polygon containing the pixels used as samples**Table 2** Random forest confusion matrix

	Predicted classes			
	Landslide	Non-landslide	Water	Total
<i>Actual classes</i>				
Landslide	2547	919	250	3716
Non-landslide	221	6226	681	7128
Water	3	50	1587	1640
Total	2771	7195	2518	12,484

Table 3 Accuracy evaluation of testing samples for unsupervised and supervised classification

	Unsupervised		Supervised	
	User's Accuracy (%)	Producer's Accuracy (%)	User's Accuracy (%)	Producer's Accuracy (%)
Landslide	74.80	52.90	91.91	68.54
Non-landslide	78.67	90.69	86.53	87.34
Water			63.02	96.76
Overall acc.		74.94 %	Overall acc.	82.98 %
Kappa coeff.		K = 0.458	Kappa coeff.	K = 0.706

The producer accuracy indicates the number of correctly classified samples divided by the total number of samples for a given class, while the user accuracy indicates the number of correctly classified samples divided by the total number of samples

**Fig. 15** RF supervised classification map

6 Conclusion

In this paper we presented a new approach for the assessment of building damage and the classification of triggered landslides shortly after a combined seismic and flooding event.

The proposed building damage assessment is based on a texture analysis of VHR SAR data in integration with rapid building surveys. From the application of this approach to the

urban area of Les Cayes, which was impacted by the 2021 Haiti earthquake, we concluded that:

- Entropy and homogeneity texture features show a good correlation with observed damage;
- A city block-level classification based on entropy can provide a rapid overview of the extension of damage in different urban areas, as confirmed by visual comparison with the StEER/GHI Fulcrum records and drone-based orthophotos;
- The city block-level classification is a convenient approach for regions where no accurate building footprint maps are available, providing that the effect of vegetation is removed from the analysis.

The proposed landslide classification is based on backscatter intensity SAR data in combination with optical-based landslide inventories, and includes separation between landslide and flooded areas. Results of the application to landslides which were triggered by the 2021 Haiti Earthquake and Tropical Cyclone Grace showed that:

- While limited by the cloud coverage, results of optical-based landslide inventories are useful to validate the proposed automated classification based on amplitude-ratio image;
- Unsupervised classification of intensity ratio images can provide a rapid identification of landslide boundaries in all weather conditions, although they are not always able to distinguish between landslides and non-landslide areas with water;
- Supervised classification of intensity ratio images provides a better accuracy in distinguishing between landslides and flooded areas, and is therefore recommended in case of concurrent earthquake and flooding hazards.

Through the integration between advanced remote sensing methods and field data, the proposed approach contributes to the advance of hybrid post-disaster missions for the assessment of earthquake-induced damage and cascading geological hazards.

Acknowledgements We thank the European Space Agency for providing Sentinel-1 and Sentinel-2 data over Haiti. SAR imagery was provided by Capella Space, under the Capella Space Open Data Community Program.

Funding VM was supported by the Dutch Research Council (NWO), project OCENW.XS5.114. StEER and GHI Data collection was supported by the National Science Foundation (NSF) under Grant CMMI-1841667, the U.S. Geological Survey (USGS) and the U.S. Agency for International Development (USAID), under USGS Cooperative Agreement No. G21AC10343-00 and USAID Award AID-OFDA-T-16-00001, under lead investigator Janise Rodgers.

Declarations

Conflict of interest The authors have not disclosed any competing interests.

Open Access This article is licensed under a Creative Commons Attribution 4.0 International License, which permits use, sharing, adaptation, distribution and reproduction in any medium or format, as long as you give appropriate credit to the original author(s) and the source, provide a link to the Creative Commons licence, and indicate if changes were made. The images or other third party material in this article are included in the article's Creative Commons licence, unless indicated otherwise in a credit line to the material. If material is not included in the article's Creative Commons licence and your intended use is not permitted by statutory regulation or exceeds the permitted use, you will need to obtain permission directly from the copyright holder. To view a copy of this licence, visit <http://creativecommons.org/licenses/by/4.0/>.

References

Adams BJ, Mansouri B, Huyck CK (2005) Streamlining post-earthquake data collection and damage assessment for the 2003 Bam, Iran, earthquake using VIEWSTM (visualizing impacts of earthquakes with satellites). *Earthq Sp* 21(1_suppl):213–218. <https://doi.org/10.1193/1.2098588>

Aimaiti Y, Liu W, Yamazaki F et al (2019) Earthquake-induced landslide mapping for the 2018 Hokkaido eastern Iburi earthquake using Palsar-2 data. *Rem Sens* 11(20):2351

Aktas YD, Ioannou I, Malcioglu FS et al (2020) (2022) Hybrid reconnaissance mission to the 30 October 2020 Aegean sea earthquake and tsunami (Izmir, Turkey and Samos, Greece): description of data collection methods and damage. *Front Built Environ* 8:1–24. <https://doi.org/10.3389/fbuil.2022.840192>

Amatya P, Kirschbaum D, Stanley T et al (2021) Landslide mapping using object-based image analysis and open source tools. *Eng Geol* 282(106):1060000. <https://doi.org/10.1016/j.engeo.2021.106000>

An L, Zhang J, Gong L, et al (2016) Integration of SAR image and vulnerability data for building damage degree estimation. In: 2016 IEEE International Geoscience and Remote Sensing Symposium (IGARSS), pp 4263–4266. <https://doi.org/10.1109/IGARSS.2016.7730111>

Bai Y, Adriano B, Mas E et al (2017) Object-based building damage assessment methodology using only post event ALOS-2/PALSAR-2 dual polarimetric SAR intensity images. *J Disaster Res* 12(2):259–271. <https://doi.org/10.20965/jdr.2017.p0259>

Bianchini S, Cigna F, Righini G et al (2012) Landslide hotspot mapping by means of Persistent Scatterer Interferometry. *Environ Earth Sci* 67:1155–1172. <https://doi.org/10.1007/s12665-012-1559-5>

Breiman L (2001) Random forests. *Mach Learn* 45:5–32. <https://doi.org/10.1023/A:1010933404324>

Burrows K, Walters RJ, Milledge D et al (2019) A new method for large-scale landslide classification from satellite radar. *Rem Sens* 11(3):237

Calais E, Symithe S, Lépinay BMD (2022) Geodetic evidence for a significant component of shortening along the northern Caribbean strike-slip plate boundary in southern Haiti. In: EGU general assembly 2022, Vienna, Austria, <https://doi.org/10.5194/egusphere-egu22-10329>

Close O, Petit S, Beaumont B et al (2021) Evaluating the potentiality of sentinel-2 for change detection analysis associated to LULUCF in Wallonia, Belgium. *Land*. <https://doi.org/10.3390/land10010055>

Cobum A, Spence J, Pomonis A (1992) Factors determining human casualty levels in earthquakes: Mortality prediction in building collapse. In: Proceedings of the 10th World Conference on Earthquake Engineering, vol 10. Balkema, Rotterdam, pp 5989–5994

Colesanti C, Wasowski J (2006) Investigating landslides with space-borne Synthetic Aperture Radar (SAR) interferometry. *Eng Geol* 88(3):173–199. <https://doi.org/10.1016/j.engeo.2006.09.013>

Corbane C, Carrion D, Lemoine G et al (2011) Comparison of damage assessment maps derived from very high spatial resolution satellite and aerial imagery produced for the Haiti 2010 earthquake. *Earthq Sp* 27(1):199–218. <https://doi.org/10.1193/1.3630223>

Cui LP, Wang XP, Dou AX et al (2018) High resolution SAR imaging employing geometric features for extracting seismic damage of buildings. *Int Arch Photogramm Rem Sens Spat Inf Sci* XLII-3:239–244. <https://doi.org/10.5194/isprs-archives-XLII-3-239-2018>

Dell'Acqua F, Polli DA (2011) Post-event only VHR radar satellite data for automated damage assessment. *Photogramm Eng Rem Sens* 77(10):1037–1043. <https://doi.org/10.14358/PERS.77.10.1037>

Dempster AP, Laird NM, Rubin DB (1977) Maximum likelihood from incomplete data via the EM algorithm. *J R Stat Soc Ser B (Methodol)* 39(1):1–38

Dong L, Shan J (2013) A comprehensive review of earthquake-induced building damage detection with remote sensing techniques. *ISPRS J Photogramm Rem Sens* 84:85–99. <https://doi.org/10.1016/j.isprsjprs.2013.06.011>

Deekhaut MVD, Poesen J, Verstraeten G et al (2007) Use of Lidar-derived images for mapping old landslides under forest. *Earth Surf Process Landf* 32(5):754–769. <https://doi.org/10.1002/esp.1417>

Ehrlich D, Guo H, Molch K et al (2009) Identifying damage caused by the 2008 Wenchuan earthquake from VHR remote sensing data. *Int J Digit Earth* 2(4):309–326. <https://doi.org/10.1080/17538940902767401>

Fan Y, Wen Q, Wang W et al (2017) Quantifying disaster physical damage using remote sensing data: a technical work flow and case study of the 2014 Ludian earthquake in China. *Int J Disaster Risk Sci* 8:471–488. <https://doi.org/10.1007/s13753-017-0143-8>

Frankel A, Harmsen S, Mueller C et al (2011) Seismic hazard maps for Haiti. *Earthq Sp* 27(1_suppl 1):23–41. <https://doi.org/10.1193/1.3631016>

Froude MJ, Petley DN (2018) Global fatal landslide occurrence from 2004 to 2016. *Nat Hazards Earth Syst Sci* 18(8):2161–2181. <https://doi.org/10.5194/nhess-18-2161-2018>

Gamba P, Casciati F (1998) GIS and image understanding for near-real-time earthquake damage assessment. *Photogramm Eng Rem Sens* 64:987–994

GDAL/OGR contributors (2020) GDAL/OGR Geospatial Data Abstraction software Library. Open Source Geospatial Foundation, <https://gdal.org>

Ge P, Gokon H et al (2019) Building damage assessment using intensity SAR data with different incidence angles and longtime interval. *J Disaster Res* 14(3):456–465. <https://doi.org/10.20965/jdr.2019.p0456>

Ge P, Gokon H, Meguro K (2020) A review on Synthetic Aperture Radar-based building damage assessment in disasters. *Rem Sens Environ* 240(11):693. <https://doi.org/10.1016/j.rse.2020.111693>

GEE (2022) Google Earth Engine guide. <https://developers.google.com/earth-engine/guides/sentinel1>

Gong L, Wang C, Wu F et al (2016) Earthquake-induced building damage detection with post-event sub-meter VHR TerraSAR-X staring spotlight imagery. *Rem Sens*. <https://doi.org/10.3390/rs8110887>

Greif V, Vlcko J (2012) Monitoring of post-failure landslide deformation by the PS-InSAR technique at Lubietova in central Slovakia. *Environ Earth Sci* 66:1585–1595. <https://doi.org/10.1007/s12665-011-0951-x>

HaitiData (2021) HaitiData. <https://haitidata.org>

Hall-Beyer M (2017) Practical guidelines for choosing GLCM textures to use in landscape classification tasks over a range of moderate spatial scales. *Int J Rem Sens* 38(5):1312–1338. <https://doi.org/10.1080/01431161.2016.1278314>

Handwerger A, Huang M, Fielding E et al (2019) A shift from drought to extreme rainfall drives a stable landslide to catastrophic failure. *Sci Rep*. <https://doi.org/10.1038/s41598-018-38300-0>

Handwerger AL (2022) GEE scripts for Handwerger et al 2022 NHESS. GitHub [code]. https://github.com/alhandwerger/GEE_scripts_for_Handwerger_et_al_2022_NHESS

Handwerger AL, Huang MH, Jones SY et al (2022) Generating landslide density heatmaps for rapid detection using open-access satellite radar data in Google Earth Engine. *Natl Hazards Earth Syst Sci* 22(3):753–773. <https://doi.org/10.5194/nhess-22-753-2022>

Haralick RM, Shanmugam KS, Dinstein I (1973) Textural features for image classification. *IEEE Trans Syst Man Cybern* 3:610–621

Harp E, Jibson R (1996) Landslides triggered by the 1994 Northridge, California, earthquake. *Bull Seismol Soc Am* 86:S319–S332

Hilley GE, Bürgmann R, Ferretti A et al (2004) Dynamics of slow-moving landslides from permanent Scatterer analysis. *Science* 304(5679):1952–1955. <https://doi.org/10.1126/science.1098821>

Höhlbling D, Friedl B, Eisank C (2015) An object-based approach for semi-automated landslide change detection and attribution of changes to landslide classes in northern Taiwan. *Earth Sci Inform* 8:327–335. <https://doi.org/10.1007/s12145-015-0217-3>

Huang MH, Fielding EJ, Liang C et al (2017) Coseismic deformation and triggered landslides of the 2016 mw 6.2 Amatrice earthquake in Italy. *Geophys Res Lett* 44(3):1266–1274. <https://doi.org/10.1002/2016GL071687>

Intrieri E, Raspini F, Fumagalli A et al (2018) The Maoxian landslide as seen from space: detecting precursors of failure with Sentinel-1 data. *Landslides* 15:123–133. <https://doi.org/10.1007/s10346-017-0915-7>

Janalipour M, Taleai M (2017) Building change detection after earthquake using multi-criteria decision analysis based on extracted information from high spatial resolution satellite images. *Int J Rem Sens* 38(1):82–99. <https://doi.org/10.1080/01431161.2016.1259673>

Jones J, Stokes M, Boulton S et al (2020) Coseismic and monsoon-triggered landslide impacts on remote trekking infrastructure, Langtang valley, Nepal. *Q J Eng Geol Hydrogeol* 53(2):159–166

Jones J, Boulton S, Stokes M et al (2021) 30-year record of Himalaya mass-wasting reveals landscape perturbations by extreme events. *Nat Commun*. <https://doi.org/10.1038/s41467-021-26964-8>

Jones JN, Boulton SJ, Bennett GL et al (2021) Temporal variations in landslide distributions following extreme events: implications for landslide susceptibility modeling. *J Geophys Res: Earth Surf* 126(7):e2021JF006067. <https://doi.org/10.1029/2021JF006067>

Joyce KE, Belliss SE, Samsonov SV et al (2009) A review of the status of satellite remote sensing and image processing techniques for mapping natural hazards and disasters. *Prog Phys Geogr: Earth Environ* 33(2):183–207. <https://doi.org/10.1177/030913309339563>

Kijewski-Correa T, AlHawamdeh B, Arteta C, et al (2021) Steer: M7.2 Nippes, Haiti earthquake preliminary virtual reconnaissance report (PVRR). Tech. rep., DesignSafe-CI, StEER, <https://doi.org/10.17603/h7vg-5691>

Kijewski-Correa T, Rodgers J, Presuma L, et al (2022) Building performance in the Nippes, Haiti earthquake: lessons learned from a hybrid response model. In: National Conference in Earthquake Engineering, Earthquake Engineering, Research Institute, Salt Lake City

Konishi T, Suga Y (2018) Landslide detection using Cosmo-Skymed images: a case study of a landslide event on Kii Peninsula, Japan. *Eur J Rem Sens* 51(1):205–221. <https://doi.org/10.1080/22797254.2017.1418185>

Kuny S, Hammer H, Schulz K (2015) Discriminating between the sar signatures of debris and high vegetation. In: 2015 IEEE International Geoscience and Remote Sensing Symposium (IGARSS), pp 473–476. <https://doi.org/10.1109/IGARSS.2015.7325803>

Lacroix P, Bièvre G, Pathier E et al (2018) Use of sentinel-2 images for the detection of precursory motions before landslide failures. *Rem Sens Environ* 215:507–516. <https://doi.org/10.1016/j.rse.2018.03.042>

Lu P, Qin Y, Li Z et al (2019) Landslide mapping from multi-sensor data through improved change detection-based Markov random field. *Rem Sens Environ* 231(11):235. <https://doi.org/10.1016/j.rse.2019.111235> (www.sciencedirect.com/science/article/pii/S0034425719302548)

Ma HR, Cheng X, Chen L et al (2016) Automatic identification of shallow landslides based on Worldview2 remote sensing images. *J Appl Rem Sens* 10(1):016008. <https://doi.org/10.1117/1.JRS.10.016008>

Marano K, Wald D, Allen T (2010) Global earthquake casualties due to secondary effects: a quantitative analysis for improving rapid loss analyses. *Nat Hazards* 52:319–328. <https://doi.org/10.1007/s11069-009-9372-5>

Marc O, Hovius N (2015) Amalgamation in landslide maps: effects and automatic detection. *Natl Hazards Earth Syst Sci* 15(4):723–733. <https://doi.org/10.5194/nhess-15-723-2015>

Marc O, Hovius N, Meunier P et al (2015) Transient changes of landslide rates after earthquakes. *Geology* 43(10):883–886. <https://doi.org/10.1130/G36961.1>. arxiv.org/abs/pubs.geoscienceworld.org/gsa/geology/article-pdf/43/10/883/3547707/883.pdf

Martinez S, Allstadt K, Slaughter S, et al (2021) Landslides triggered by the august 14, 2021, magnitude 7.2 Nippes, Haiti, earthquake. Open-file report, U.S. Geological Survey, <https://doi.org/10.3133/of20211112>

Massey C, Townsend D, Lukovic B et al (2020) Landslides triggered by the mw 7.8 14 November 2016 Kaikoura earthquake: an update. *Landslides* 17:2401–2408. <https://doi.org/10.1007/s10346-020-01439-x>

Matsuoka M, Koshimura S, Nojima N (2010) Estimation of building damage ratio due to earthquakes and tsunamis using satellite SAR imagery. In: 2010 IEEE International Geoscience and Remote Sensing Symposium, pp 3347–3349, <https://doi.org/10.1109/IGARSS.2010.5650550>

Maurer J, Dutta R, Vernon A et al (2022) Complex rupture and triggered aseismic creep during the 14 august 2021 Haiti earthquake from satellite geodesy. *Geophys Res Lett* 49(11):e2022GL098573. <https://doi.org/10.1029/2022GL098573>

McFeeters SK (1996) The use of the normalized difference water index (NDWI) in the delineation of open water features. *Int J Rem Sens* 17(7):1425–1432. <https://doi.org/10.1080/01431169608948714>

Meslem A, Yamazaki F, Maruyama Y (2011) Accurate evaluation of building damage in the 2003 Boumerdes, Algeria earthquake from Quickbird satellite images. *J Earthq Tsunami* 05(01):1–18. <https://doi.org/10.1142/S1793434111001029>

Microsoft (2023) Microsoft global building footprints. <https://github.com/microsoft/GlobalMLBuildingFootprints>

Miranda E (2021) Assessment manual: Rapid damage classification for Nippes august 14, 2021 m7.2 earthquake in Haiti. Tech. rep

Mondini A, Guzzetti F, Reichenbach P et al (2011) Semi-automatic recognition and mapping of rainfall induced shallow landslides using optical satellite images. *Rem Sens Environ* 115(7):1743–1757. <https://doi.org/10.1016/j.rse.2011.03.006> (www.sciencedirect.com/science/article/pii/S0034425711000836)

Mondini AC, Santangelo M, Rocchetti M et al (2019) Sentinel-1 SAR amplitude imagery for rapid landslide detection. *Rem Sens*. <https://doi.org/10.3390/rs11070760>

Okuwaki R, Fan W (2022) Oblique convergence causes both thrust and strike-slip ruptures during the 2021 m 7.2 Haiti earthquake. *Geophys Res Lett* 49(2):e2021GL096373. <https://doi.org/10.1029/2021GL096373>

OSM (2021) Openstreetmap. <https://www.openstreetmap.org>

Parker RN, Hancox GT, Petley DN et al (2015) Spatial distributions of earthquake-induced landslides and hillslope preconditioning in the northwest south Island, New Zealand. *Earth Surface Dyn* 3(4):501–525. <https://doi.org/10.5194/esurf-3-501-2015>

Rabby Y, Li Y (2019) An integrated approach to map landslides in Chittagong hilly areas, Bangladesh, using google earth and field mapping. *Landslides* 16:633–645. <https://doi.org/10.1007/s10346-018-1107-9>

Rau JY, Jhan JP, Rau RJ (2014) Semiautomatic object-oriented landslide recognition scheme from multisensor optical imagery and dem. *IEEE Trans Geosci Rem Sens* 52(2):1336–1349. <https://doi.org/10.1109/TGRS.2013.2250293>

Reichenbach P, Rossi M, Malamud BD et al (2018) A review of statistically-based landslide susceptibility models. *Earth-Sci Rev* 180:60–91. <https://doi.org/10.1016/j.earscirev.2018.03.001>

Roback K, Clark MK, West AJ et al (2018) The size, distribution, and mobility of landslides caused by the 2015 mw7.8 Gorkha earthquake, Nepal. *Geomorphology* 301:121–138. <https://doi.org/10.1016/j.geomorph.2017.01.030>

Roberts S, Jones JN, Boulton SJ (2021) Characteristics of landslide path dependency revealed through multiple resolution landslide inventories in the Nepal Himalaya. *Geomorphology* 390(107):868. <https://doi.org/10.1016/j.geomorph.2021.107868>

Robinson T, Rosser N, Walters R (2019) The spatial and temporal influence of cloud cover on satellite-based emergency mapping of earthquake disasters. *Sci Rep*. <https://doi.org/10.1038/s41598-019-49008-0>

Robinson TR, Rosser NJ, Densmore AL et al (2017) Rapid post-earthquake modelling of coseismic landslide intensity and distribution for emergency response decision support. *Natl Hazards Earth Syst Sci* 17(9):1521–1540. <https://doi.org/10.5194/nhess-17-1521-2017>

Saint Fleur N, Klinger Y, Feuillet N (2020) Detailed map, displacement, paleoseismology, and segmentation of the enriquillo-plantain garden fault in Haiti. *Tectonophysics* 778(228):368. <https://doi.org/10.1016/j.tecto.2020.228368>

Saito K, Spence R, de Foley CTA (2005) Visual damage assessment using high-resolution satellite images following the 2003 bam, Iran, earthquake. *Earthq Sp* 21(1_suppl):309–318. <https://doi.org/10.1193/1.2101107>

Samia J, Temme A, Bregt A et al (2017) Do landslides follow landslides? Insights in path dependency from a multi-temporal landslide inventory. *Landslides* 14:547–558

Scheip CM, Wegmann KW (2021) Hazmapper: a global open-source natural hazard mapping application in Google Earth Engine. *Natl Hazards Earth Syst Sci* 21(5):1495–1511. <https://doi.org/10.5194/nhess-21-1495-2021>

Schlögel R, Doubre C, Malet JP et al (2015) Landslide deformation monitoring with ALOS/PALSAR imagery: a D-InSAR geomorphological interpretation method. *Geomorphology* 231:314–330. <https://doi.org/10.1016/j.geomorph.2014.11.031>

Schweier C, Markus M (2006) Classification of collapsed buildings for fast damage and loss assessment. *Bull Earthq Eng* 4(2):177–192. <https://doi.org/10.1007/s10518-006-9005-2>

Sharma RC, Tateishi R, Hara K et al (2017) Earthquake Damage Visualization (EDV) technique for the rapid detection of earthquake-induced damages using SAR data. *Sensors*. <https://doi.org/10.3390/s17020235>

SNAP (2022) S1TBX ESA Sentinel Application Platform. <http://step.esa.int>

Stringham C, Farquharson G, Castelletti D, et al (2019) The capella x-band sar constellation for rapid imaging. In: IGARSS 2019 - 2019 IEEE International Geoscience and Remote Sensing Symposium, pp 9248–9251, <https://doi.org/10.1109/IGARSS.2019.8900410>

Stumpf A, Kerle N (2011) Object-oriented mapping of landslides using random forests. *Rem Sens Environ* 115(10):2564–2577. <https://doi.org/10.1016/j.rse.2011.05.013>

Ocha UN (2021) Global humanitarian overview: Haiti. Tech. rep, United Nations

UNDP (2015) Human development report 2015. UNDP (United Nations Development Programme) <http://report2015.archive.s3-website-us-east-1.amazonaws.com>

UNITAR (2020) Programme performance report for the biennium 2018–2019. Tech. rep, United Nations Institute for Training and Research

USGS (2022) Earth explorer, <https://earthexplorer.usgs.gov>

Whitworth MR, Giardina G, Penney C et al (2022) Lessons for remote post-earthquake reconnaissance from the 14 August 2021 Haiti earthquake. *Front Built Environ* 8(April):1–16. <https://doi.org/10.3389/fbui.2022.873212>

Williams JG, Rosser NJ, Kincey ME et al (2018) Satellite-based emergency mapping using optical imagery: experience and reflections from the 2015 Nepal earthquakes. *Natl Hazards Earth Syst Sci* 18(1):185–205. <https://doi.org/10.5194/nhess-18-185-2018>

Wu F, Gong L, Wang C et al (2016) Signature analysis of building damage with TerraSAR-X new staring spotlight mode data. *IEEE Geosci Rem Sens Lett* 13(11):1696–1700. <https://doi.org/10.1109/LGRS.2016.2604841>

Yamazaki F, Yano Y, Matsuoka M (2005) Visual damage interpretation of buildings in Bam city using quickbird images following the 2003 bam, Iran, earthquake. *Earthq Sp* 21(1_suppl):329–336. <https://doi.org/10.1193/1.2101807>

Yun SH, Hudnut K, Owen S et al (2015) Rapid damage mapping for the 2015 Mw 7.8 Gorkha earthquake using synthetic aperture radar data from COSMO-SkyMed and ALOS-2 satellites. *Seismol Res Lett* 86(6):1549–1556. <https://doi.org/10.1785/0220150152>

Yusuf Y, Matsuoka M, Yamazaki F (2001) Damage assessment after 2001 Gujarat earthquake using Landsat-7 satellite images. *J Indian Soc Rem Sens* 29:17–22. <https://doi.org/10.1007/BF02989909>

Zhao L, Yang J, Li P et al (2013) Damage assessment in urban areas using post-earthquake airborne POL-SAR imagery. *Int J Rem Sens* 34(24):8952–8966. <https://doi.org/10.1080/01431161.2013.860566>

Publisher's Note Springer Nature remains neutral with regard to jurisdictional claims in published maps and institutional affiliations.

Authors and Affiliations

Giorgia Giardina¹  · **Valentina Macchiarulo**¹ · **Fatemeh Foroughnia**¹ ·
Joshua N. Jones² · **Michael R. Z. Whitworth**² · **Brandon Voelker**³ · **Pietro Milillo**^{3,4} ·
Camilla Penney⁵ · **Keith Adams**⁶ · **Tracy Kijewski-Correa**⁷

✉ Giorgia Giardina
g.giardina@tudelft.nl

¹ Department of Geoscience and Engineering, Delft University of Technology, Stevinweg 1, 2628 CN Delft, The Netherlands

² AECOM, Tailyour Road, Plymouth PL6 5DH, UK

³ Department of Civil and Environmental Engineering, University of Houston, 4226 Martin Luther King Blvd, Houston, TX 77204, USA

⁴ Microwaves and Radar Institute, German Aerospace Center (DLR), Münchener Straße 20, 82234 Weßling, Germany

⁵ Te Kura Aronukurangi, School of Earth and Environment, Te Whare Wānanga o Waitaha, University of Canterbury, Ilam Road, Christchurch 8041, Aotearoa, New Zealand

⁶ College of Engineering, Design and Physical Sciences, Brunel University London, Kingston Lane, Uxbridge UB8 3PH, UK

⁷ College of Engineering and Keough School of Global Affairs, University of Notre Dame, 3150 Jenkins Nanovic Halls, Notre Dame, IN 46556, USA